Available online at www.sciencedirect.com
SCIENCE DIRECT
ELSEVIER
International Journal of Thermal Sciences 43 (2004) 1171–1180
International Journal of Thermal Sciences
www.elsevier.com/locate/ijts

Crystallization of supercooled spherical nodules in a flow

Kamal El Omari, Jean Pierre Dumas *

Laboratoire de thermique, énergétique et procédés, avenue de l'Université, BP 1155, 64013 Pau, France

Received 21 November 2003; received in revised form 19 March 2004; accepted 26 April 2004

Abstract

The general context of this work concerns the latent heat storage (cold storage) by encapsulated spherical nodules of 7.7 cm in diameter containing a Phase Change Material (PCM) and filling a cylindrical tank (about 2500 nodules per m^3). During the storage process, a cold heat transfer liquid flows through the tank to crystallize the PCM inside the nodules. The stored energy is released when a hotter heat transfer liquid flows through the tank to induce the melting of the PCM. As the velocity in the tank is relatively small (a few mm·s^{-1}), natural convection is expected on the coolant when the latent heat is released at the crystallization of the PCM. The present study concerns a single nodule surrounded by a flowing heat transfer liquid at a temperature T_C lower than the melting temperature T_F. This text presents an enthalpic modelling of the phase change inside the nodule coupled with a CFD simulation of the external flow to describe the mutual influence of the natural convection and the kinetics of crystallization. This study is afterwards extended to the case of two superposed nodules to investigate the influence of the crystallization of the lower nodule on the upper one.

Keywords: Latent heat storage; Encapsulated spherical nodules; Supercooling; Crystallization; Natural convection

1. Introduction

During the heat storage process studied in this paper, a coolant fluid flows through a heat storage tank and induces the crystallization of a phase change material (PCM) contained in spherical nodules. On cooling, the phase change of the PCM does not occur at its melting temperature T_F (273.15 K for the investigated nodules: the PCM being water), but several degrees lower, because of the phenomenon of supercooling. In industrial applications, the consequence of this phenomenon is very important, inducing supplementary cooling and therefore the use of a higher power refrigerating machine. The addition of nucleating agents reduces this supercooling but does not eliminate it [1].

While the discharge process (PCM melting) occurs at the melting temperature (thermodynamic equilibrium), the kinetics of the storage process (PCM freezing) depends on the nucleation law of the supercooled liquid which has an erratic character described by probabilistic laws. By using these laws in the case of a vertical flow, a model that predicts the temporal evolution of the temperature in each point of the tank has been validated by experiments [1,2]. It was a global study of the behavior of the tank without differentiating the nodules, however, it highlighted the difference between the storage (cooling) and the discharge (heating) due to the supercooling phenomenon.

At the scale of a nodule, the crystallization after the supercooling results in a difference of temperature between the external surface of this nodule and the surrounding fluid. This difference of temperature induces natural convection streams changing completely the flow patterns of the initial forced convection within the coolant fluid and modifying the wall heat flux.

The inward solidification of spheres has received considerable attention. Numerical studies were mainly semi-analytical and one-dimensional [3–7] solving the Stefan problem. Some of these models neglected the sensible heat against the latent one [8], and most of them did not take into account the supercooling phenomenon. The boundary conditions used in these studies were a fixed temperature or a fixed heat transfer coefficient. Experimental studies described the behavior of a single nodule [9,10] or of a whole PCM-thermal-storage system using spherical capsules [2, 10–12]. Such storage systems have been also simulated by

---

* Corresponding author.
E-mail addresses: kamal.elomari@univ-pau.fr (K. El Omari), jean-pierre.dumas@univ-pau.fr (J.P. Dumas).

1290-0729/$ – see front matter © 2004 Elsevier SAS. All rights reserved.
doi:10.1016/j.ijthermalsci.2004.04.007

Nomenclature

c	specific heat	$\mathrm{J \cdot kg^{-1} \cdot K^{-1}}$
D	external diameter of nodule	m
f	liquid fraction	
Gr	Grashof number, $= \frac{g\beta\Delta T D^3}{\nu^2}$	
g	gravitational acceleration, $= 9.81$	$\mathrm{m \cdot s^{-2}}$
h	specific enthalpy	$\mathrm{J \cdot kg^{-1}}$
H	enthalpy	J
k	thermal conductivity	$\mathrm{W \cdot K^{-1} \cdot m^{-1}}$
L	latent heat of fusion	$\mathrm{J \cdot kg^{-1}}$
m_α	mass of the $\square_\alpha$ phase of the PCM	kg
M	total mass of PCM	kg
Nu	Nusselt number, $= \frac{\varphi D}{k \Delta T}$	
Pr	Prandtl number, $= \frac{\rho \nu c}{k}$	
R_e	external radius of the nodule, $= D/2 = 0.0385$	m
R_i	internal radius of the nodule, $= 0.0365$	m
T_C	temperature of crystallization and of the coolant fluid	K
T_F	melting temperature	K
T_P	temperature of external surface of nodule	K
U	inflow velocity	$\mathrm{m \cdot s^{-1}}$
u, v	velocity vector $\vec{V}$ components according to (x, r) coordinates (Fig. 2)	
μ	dynamic viscosity of the outer fluid	$\mathrm{kg \cdot m^{-1} \cdot s^{-1}}$
ν	kinematic viscosity of the outer fluid	$\mathrm{m^2 \cdot s^{-1}}$
β	volumetric thermal expansion coefficient	$\mathrm{K^{-1}}$
φ	heat flux	$\mathrm{W \cdot m^{-2}}$
ψ	stream function	$\mathrm{kg \cdot s^{-1}}$
θ	angular position varying from the bottom to the top (Fig. 4)	rad
ρ	density	$\mathrm{kg \cdot m^{-3}}$

Subscripts

$\square_L$	liquid PCM phase
$\square_S$	solid PCM phase
$\square_P$	envelope of nodule
$\square_f$	coolant fluid

global models which use one-nodule modelling as those presented above.

The present study investigates the case of a single nodule previously maintained at a temperature below the melting point by a liquid flowing vertically around it. At time $t = 0$, the crystallization starts (metastability breakdown) inducing a sudden energy release that results in natural convection. The kinetics of the crystallization depends on the resulting heat transfer. So, there is a mutual influence between the phase change and the flow around the nodule. The external coolant liquid flow is simulated by a CFD code to determine the local heat exchange while the crystallization is resolved by an original code using a two-dimensional enthalpy method. These two different calculations are linked when their boundary conditions are expressed.

2. Flow around a nodule

Heat transfer from a sphere to air flow by mixed convection has been studied experimentally for the case of aiding, opposing and cross flow by Yuge [13] and Armaly et al. [14]. Amato and Tien [15] studied natural convection to water. The results of these works were formulated on empirical correlations. Churchill [16] has proposed more generalized correlation equations concerning free convection, giving the mean Nusselt number as a function of Prandtl and Grashof numbers which were in good agreement with most of the previous experimental data. Kirk and Johnson [17] presented an experimental study of mixed convection to air, investigating aiding, opposing and cross flows. They highlighted the differences between, on the one hand, aiding and cross flows and on the other hand opposing flow. They showed that the variation of the Nusselt number of opposing flow against the Reynolds number presents local maximum and minimum at some moderated values of Re. Tang and Johnson [18] presented a visualization study to explain this phenomenon. Tang et al. [19] derived an empirical formulation that describes opposing flow heat convection.

Most of experimental studies of free and mixed convection were concerned with air flow. This was also the case of numerical studies which used on a large part the boundary layer type modelling [20,21] or the stream function-vorticity formulation [22–24]. They analyzed the respective influence of forced and natural streams on the mixed convection with respect to the buoyancy parameter Gr/Re^2.

The flows studied in the present work are characterized by large buoyancy parameters, due to small Reynolds numbers as presented below.

2.1. Flow characteristics

In heat storage tank, two different flows are possible (Fig. 1):

- The *normal mode* (aiding or assisting flow), where the forced flow is vertically rising in the same direction as the natural convection.
- The *inverse mode* (opposing flow), where the forced flow is vertically descending in the direction opposite to that of the free convection.

The tanks generally installed in the storage loop have relatively large volumes (from 20 to 500 $\mathrm{m^3}$) with sections a few $\mathrm{m^2}$ in area. The duration of a complete storage operation

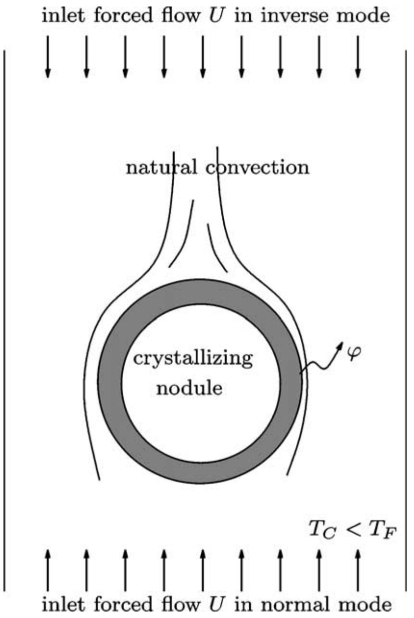

Fig. 1. General sketch of the flow.

is about several hours. So, the mean velocity of the coolant liquid is very low (6×10^{-4}–3×10^{-3} m·s^{-1}), thus, we will only consider this range of velocity. The Reynolds number based on the nodule diameter

$$5 \leqslant Re = \frac{UD}{\nu_f} \leqslant 35 \tag{1}$$

indicates that the forced flow is laminar. The Grashof number Gr that characterizes the natural convection due to $\Delta T = T_P - T_C$, has a maximum value of $Gr_{\max} = 9.3 \times 10^4$ [25,26]. This Gr value is relative to the maximum studied value of ΔT: $\Delta T_{\max} = 7$ K. The coolant fluid is an aqueous solution of propylene glycol which density depends on the temperature as:

$$\rho_f = 873.39 + 1.94\,T - 4.286 \times 10^{-3} T^2 \tag{2}$$

The corresponding Prandtl number is about $Pr_f = 86$. According to the value of the maximal Grashof number $Gr_{\max} < 10^9$, we consider the natural convection as fully laminar [27] and we assume the flow as axisymmetric. Moreover, the mixed convection ratio for all studied flows is:

$$20 < \frac{Gr}{Re^2} < 75$$

So, we predict in advance that the natural convection will be of major importance in the fluid flow and in the heat transfer from the nodule.

2.2. Flow simulation: Equations and numerical methods

For the simulation of the unsteady incompressible flow around the nodule, we have chosen to use the commercial code Fluent [28] based on finite volumes on unstructured grids. Unsteady two-dimensional Navier–Stokes equations including buoyancy effects are considered (the Boussinesq approximation has not been used). The conservation equations are expressed in the axisymmetrical coordinates (x,r) indicated in Fig. 2:

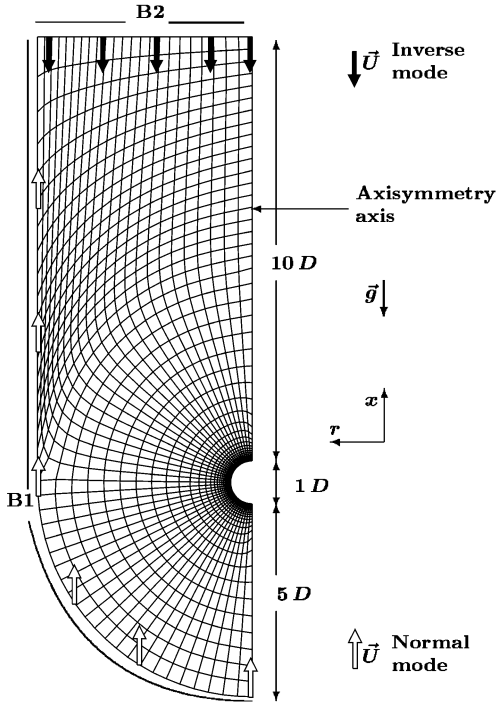

Fig. 2. Grid of the flow computational domain.

$$\frac{\partial \rho}{\partial t} + \frac{\partial}{\partial x}(\rho u) + \frac{\partial}{\partial r}(\rho v) + \frac{\rho v}{r} = 0 \tag{3}$$

$$\begin{aligned}
&\frac{\partial}{\partial t}(\rho u) + \frac{1}{r}\frac{\partial}{\partial x}(r\rho u u) + \frac{1}{r}\frac{\partial}{\partial r}(r\rho v u)\\
&\quad = -\frac{\partial p}{\partial x} + \frac{1}{r}\frac{\partial}{\partial x}\left[r\mu\left(2\frac{\partial u}{\partial x} - \frac{2}{3}(\nabla\cdot\vec{V})\right)\right]\\
&\qquad + \frac{1}{r}\frac{\partial}{\partial r}\left[r\mu\left(\frac{\partial u}{\partial r} + \frac{\partial v}{\partial x}\right)\right] - \rho g
\end{aligned} \tag{4}$$

$$\begin{aligned}
&\frac{\partial}{\partial t}(\rho v) + \frac{1}{r}\frac{\partial}{\partial x}(r\rho u v) + \frac{1}{r}\frac{\partial}{\partial r}(r\rho v v)\\
&\quad = -\frac{\partial p}{\partial r} + \frac{1}{r}\frac{\partial}{\partial x}\left[r\mu\left(\frac{\partial v}{\partial x} + \frac{\partial u}{\partial r}\right)\right]\\
&\qquad + \frac{1}{r}\frac{\partial}{\partial r}\left[r\mu\left(2\frac{\partial v}{\partial r} - \frac{2}{3}(\nabla\cdot\vec{V})\right)\right]\\
&\qquad - 2\mu\frac{v}{r^2} + \frac{2}{3}(\nabla\cdot\vec{V})
\end{aligned} \tag{5}$$

$$\begin{aligned}
&\frac{\partial(\rho E)}{\partial t} + \frac{1}{r}\left[\frac{\partial}{\partial x}\big(r\,u(\rho E + p)\big) + \frac{\partial}{\partial r}\big(r\,v\,(\rho E + p)\big)\right]\\
&\quad = \frac{1}{r}\left[\frac{\partial}{\partial x}\left(r\,k\frac{\partial T}{\partial x}\right) + \frac{\partial}{\partial r}\left(r\,k\frac{\partial T}{\partial r}\right)\right]
\end{aligned} \tag{6}$$

which are mass Eq. (3), momentum Eqs. (4), (5) and energy Eq. (6) conservation equations, where $\nabla\cdot\vec{V} = \frac{\partial u}{\partial x} + \frac{\partial v}{\partial r} + \frac{v}{r}$ and $E = h - \frac{p}{\rho} + \frac{\vec{V}^2}{2}$.

The Fluent solver employs an upwind cell-centered finite volume scheme with a discretization based on linear reconstruction having a second-order spatial accuracy [29]. Eqs. (4)–(6) are solved sequentially in a segregated manner and the continuity Eq. (3) is satisfied using the SIMPLE procedure [30]. Temporal discretization is first-order and fully implicit. The linear system obtained by the discretization of Eqs. (4)–(6) is solved by a Gauss–Seidel iteration and an algebraic multigrid procedure.

The chosen computational domain geometry is represented in Fig. 2. Most of the domain borders are set at a distance of $5D$ from the surface of the nodule in order to reduce their effects. The upper border is set at $10D$. This geometry is used to study both normal and inverse flow modes by changing the boundary conditions assigned to them.

- For normal mode calculations (assisting flow), the boundary noted **B1** in Fig. 2 is assigned an inflow condition where the velocity vector is $\vec{V}_{\text{inlet}} = U\,\vec{x} + 0\,\vec{r}$ with $U > 0$ (white arrows in Fig. 2). The boundary noted **B2** is the outflow.
- In the inverse mode (opposing flow), the fluid enters the domain through the boundary **B2** with a velocity vector $\vec{V}_{\text{inlet}} = -U\,\vec{x} + 0\,\vec{r}$ (black arrows in Fig. 2).

For both modes, the fluid temperature at the inlet is fixed at T_C, the temperature at which the nodule crystallizes. The boundary condition at the surface of the nodule is a no-slip condition ($u = v = 0$) and a prescribed time depending heat flux. This heat flux is calculated by the unsteady phase change model described in the next section.

The chosen grid was a result of a study of the sensitivity of the solution to the grid size, where, a two times finer grid did not change noticeably the solution. The chosen grid is composed of 1587 quadrilateral cells (Fig. 2). A series of computations was carried out in order to validate this grid by comparing the obtained results to available experimental data relative to heat transfer, the most influent phenomenon on the internal phase change. For example, the mean Nusselt number $\overline{Nu}$, obtained by pure natural convection computations, was compared to the Churchill correlation [16]:

$$\overline{Nu} = 2 + \frac{0.589(Gr\,Pr)^{0.25}}{[1 + (0.43/Pr)^{9/16}]^{4/9}}$$

The studied Pr was equal to 86, and the Gr range was $6 \times 10^3 \leqslant Gr \leqslant 10^5$. Obtained $\overline{Nu}$ values were less than 5% different from the correlation values over this Gr range. Also, forced convection computations were performed for a Reynolds number range of $5 \leqslant Re \leqslant 150$ including our studied range. The resulting mean Nusselt number was compared to Whitaker correlation [31] and again the difference was below 5%.

3. Crystallization of the PCM inside a spherical nodule

Spherical nodules used in heat storage tanks are often filled with water or aqueous solution. So, to prevent from the volume expansion during the freezing, an air bubble is left in the nodule. The relative elasticity of the envelope allows to fill it up to 95%. The effect of this air bubble on the crystallization of the nodule has been qualitatively described by Arnold [10]. Recently, Eames and Adref [9], investigated experimentally a sphere filled to 80% of its volume with water, and they measured the evolution of the air bubble pressure to get an estimation of the ice volume. The exact shape of the liquid–solid interface was not observed experimentally, but, the previous authors [9,10] described that, during the freezing, a thin layer of ice is formed at the free surface of water. The crystallization progresses inducing an increase of the pressure of the trapped water, so, the upper ice layer is fractured and water is released. This process is repeated until there is no liquid water. The air bubble reduces the heat transfer to the water, and prevents the formation of ice in that part of the nodule as long as it remains.

For the nodules investigated in our laboratory [1,2], the air bubble represents only 5% of the volume, so the air bubble is compressed earlier during the crystallization. Knowing that the volume of water increases by about 8.4% when freezing, we can estimate that the air volume completely disappears when 50% of the water volume crystallizes, which corresponds to 20% of the nodule radius.

For convenience, in the present study the nodule is considered as completely filled with PCM and its volume is considered as constant. So, we neglect the air bubble, and assume no variation of the density ρ at the crystallization. These two assumptions are complementary. But to take into account the effective mass of PCM, the latent heat L is reduced. We also assume that the specific heats of water c_L and ice c_S, as well as their conductivities k_L and k_S, do not depend on temperature.

3.1. Crystallization start

Before the crystallization start, the external flowing liquid and the supercooled PCM inside the sphere are at the temperature $T_C < T_F$. At the metastability breakdown, the crystallization of a first PCM layer is so quick that we can consider this transformation as adiabatic. When the first layer is formed, the temperature of the liquid increases up to the melting point T_F due to the release of energy. This sudden temperature jump at the center of the nodule was measured experimentally by Bédécarrats and Dumas [1] and by Ismail and Henríquez [12]. So:

$$\begin{aligned} H_{\text{final}} - H_{\text{initial}} &= 0 \\ &= \big[m_L h_L(T_F) + m_S h_S(T_F)\big] - (m_L + m_S) h_L(T_C) \\ &= (m_L + m_S) c_L (T_F - T_C) - m_S L \end{aligned} \tag{7}$$

The mass of the ice which has appeared is:

$$m_S = \frac{(m_L + m_S)c_L(T_F - T_C)}{L} \tag{8}$$

which corresponds to the radius of a first ice layer:

$$r_0 = R_i\left[\left(1 - \frac{\rho_L}{\rho_S}\frac{c_L}{L}(T_F - T_C)\right)\right]^{1/3} \tag{9}$$

At $t = 0$, the radius of the liquid–solid interface is not taken equal to the inner radius of the nodule R_i but to r_0 which depends on the supercooling. We can notice that because the supercooling generally observed with such a volume is relatively small (a few K), this first ice layer is very thin ($\approx 2\%\ R_i$). As stated before, we neglect the air bubble, so we assume that this first ice layer is concentric.

3.2. Enthalpic modelling of crystallization

In a previous work [26], the authors have used a quasi-stationary method to determine the kinetics of crystallization of the PCM inside the nodule. This method is relatively easy to operate but it assumes that the crystallization is concentric. It is not exactly the case because, as it can be easily predicted, the external flow is responsible of a non-uniform distribution of the heat flux on the nodule surface. So, in this paper, the modelling of the phase change is achieved by a two-dimensional axisymmetric enthalpy method. This method uses a fixed grid for representing both solid and liquid phases. The liquid fraction parameter f determines which phase is present in each cell of the grid. So, for $f = 0$, the PCM is solid, for $f = 1$, the PCM is liquid and for $0 < f < 1$, the phase of the PCM in the cell is changing. Voller gave a good presentation of this method in [32].

Inside the PCM, the equation of the of heat diffusion can be written:

$$\frac{\partial \Delta H}{\partial t} = \nabla \cdot (k\,\nabla T) \tag{10}$$

where the variation of the enthalpy:

$$\begin{aligned}\Delta H(T) &= H(T) - H(T_F)\\ &= \int_{T_F}^{T} \rho\, c(T)\,\mathrm{d}T + \rho\, f(T)\, L\end{aligned} \tag{11}$$

The liquid fraction $f(T)$ is defined by:

$$f = \begin{cases}1 & \text{if } T > T_F\\ 0 & \text{if } T < T_F\end{cases} \tag{12}$$

$$0 < f < 1 \quad \text{if } T = T_F$$

With spherical coordinates (r,θ), Eq. (10) becomes:

$$\begin{aligned}\rho c\frac{\partial T}{\partial t} &= \frac{1}{r^2}\frac{\partial}{\partial r}\left(r^2 k\frac{\partial T}{\partial r}\right)\\ &\quad + \frac{1}{r\sin\theta}\frac{\partial}{\partial \theta}\left(\frac{k}{r}\frac{\partial T}{\partial \theta}\sin\theta\right) - \rho L\frac{\partial f}{\partial t}\end{aligned} \tag{13}$$

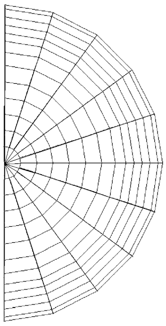

Fig. 3. Grid inside the nodule.

This equation is integrated over the control-volumes located around the grid nodes. In Fig. 3, we give the grid used inside the nodule. Indeed, the external grid (Fig. 2) and the internal one (Fig. 3), are in connection at the fluid–nodule interface.

The numerical calculation is implemented as follows:

(1) Knowing at time t, the temperatures $T_P(t,\theta)$ of the fluid–nodule interface given by the CFD code and the heat flux $\varphi(t,\theta)$, we first take into account the thermal resistance of the envelope by

$$T_N(t + \Delta t, \theta) = T_P(t,\theta) + \frac{R_e - R_i}{k_P}\varphi(t,\theta) \tag{14}$$

where k_P is the thermal conductivity of the envelope and $T_N(t + \Delta t, \theta)$ are the temperatures of the inner surface of the nodule (see Fig. 4).

(2) These temperatures $T_N(t + \Delta t, \theta)$ constitute the boundary conditions used to solve the Eq. (13) by a finite volume method. The obtained linear system is solved by a Successive Over Relaxation (SOR) method. The liquid fraction f is then corrected as suggested by Voller [32] or by Lacroix et al. [33] and a new linear system is resolved until convergence. So we obtain $T(t + \Delta t, r, \theta)$ and $f(t + \Delta t, r, \theta)$. The points of the nodule where $0 < f < 1$ precise the location of the solid–liquid interface.

(3) At $t + \Delta t$, the flux at the nodule surface is calculated by

$$\varphi(t + \Delta t, \theta) = -k_S \left.\frac{\partial T(t + \Delta t, r, \theta)}{\partial r}\right|_{R_i}$$

(4) These new values of the flux are used by the CFD code as boundary conditions at the nodule surface.

(5) The equations of conservation of mass, momentum and energy of the coolant fluid (Eqs. (3)–(6)) are resolved by this code at time $t + \Delta t$.

(6) The calculated temperatures $T_P(t + \Delta t, \theta)$ permit to begin the computations for a new time step (step (1)).

4. Results

We made calculations in different flow configurations, by varying U, the vertical component of the velocity of the

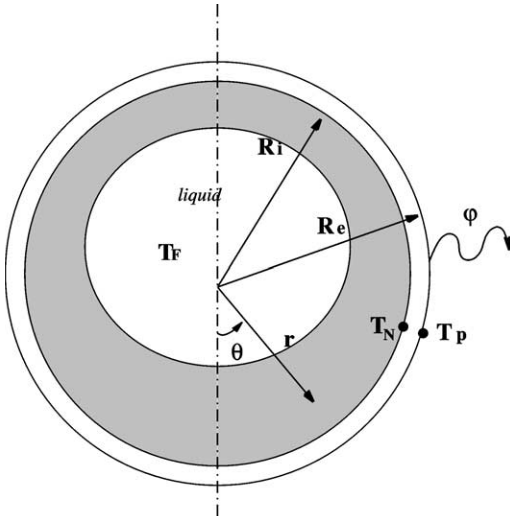

Fig. 4. Sketch of a crystallizing nodule (assuming the hypotheses of the present study).

Table 1
Studied flow configurations

Configuration	U [m·s^{-1}]	T_C [K]
7–24	0.0024	267
7–12	0.0012	267
7–48	0.0048	267
5–24	0.0024	265
9–24	0.0024	269

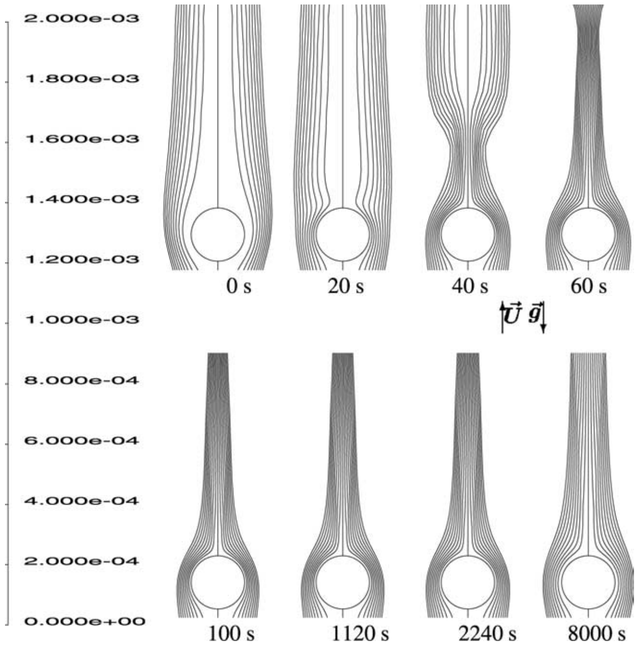

Fig. 5. Streamlines in normal mode [kg·s^{-1}]. (*The lowest ψ value is at the nodule surface.*)

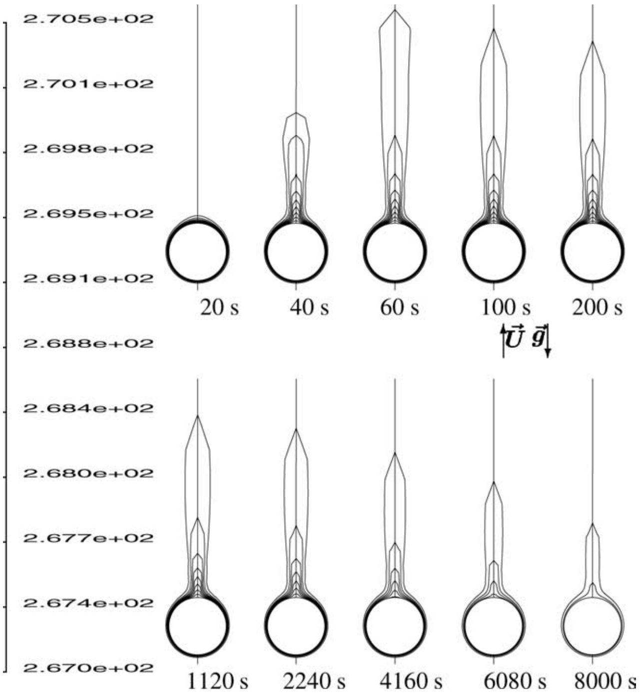

Fig. 6. Isotherms in normal mode [K]. (*The lowest T value is at the outer line.*)

coolant fluid at the inflow, as well as the temperature T_C. The different studied configurations are given in Table 1. These configurations were investigated in both normal and inverse mode.

4.1. Results concerning the flow

As an example we present the results concerning a flow at the configuration 7–12 (Table 1). The calculations start from an isothermal flow situation at T_C where only forced convection is present. In Fig. 5, we see the streamlines in the *normal mode* at different instants during the crystallization of the PCM. Just after the beginning of the crystallization, we observe an acceleration of the fluid which distort the streamlines. We noticed [25] that the axial velocity u quickly becomes very important since $u/U \approx 10$ as soon as $t = 40$ s. As confirmed in Fig. 6, where the isotherms at different instants are given, a large plume is growing along the axis.

At the same configuration 7–12, but in *inverse mode*, the streamlines exhibit quite different patterns as given in Fig. 7. This figure shows an opposition between the forced flow and the natural convection inducing swirls and recirculations of fluid. We notice that these recirculations move away from the nodule at early crystallization instants. Moreover, by examining the temperature distributions over the nodule axis, we have seen that they are quite equivalent to those obtained in the normal mode: this is due to the predominance of the natural convection as expected.

4.2. Results concerning the crystallization

As explained above, the enthalpic method allows a two-dimensional modelling of the phase change problems. So,

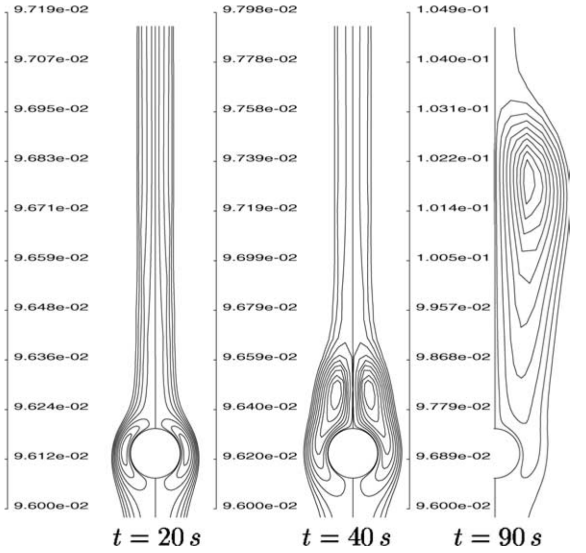

Fig. 7. Streamlines in Inverse mode [kg·s^{-1}]. (*The lowest ψ values are at the outer lines*.)

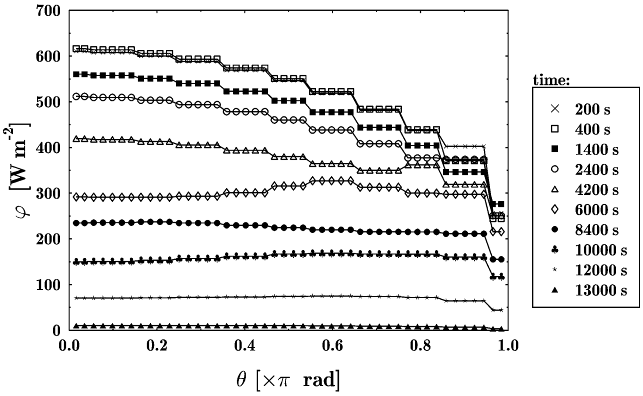

Fig. 8. Angular distribution of the local heat flux at different instants.

we plot in Fig. 8 the local heat flux at the external nodule surface versus the angle θ (Fig. 4), for the case of the configuration 7–24 of the normal mode. We notice that the exchange of energy has its highest values at the beginning of the crystallization and it decreases when the crystallization progresses. As expected, the heat flux is not uniform: it is more important at the bottom of the nodule than at the top. This is due to a smaller temperature gradient in the fluid at the top of the external surface of the nodule. This low heat flux region corresponds to the location of the air bubble that was neglected, so, we think that this reduces the error introduced by this assumption.

To compare the results for different configurations, we calculate the mean value of the heat flux given by:

$$\overline{\varphi(t)} = \frac{1}{\pi}\int_0^\pi \varphi(t,\theta)\,\mathrm{d}\theta. \tag{15}$$

In Fig. 9, we compare the mean heat fluxes relative to all the studied configurations of the normal mode. We observe that the curves have a quasi-linear shape as it has been observed experimentally [1]. We also deduce that the total duration of the crystallization, given when the heat flux vanishes, depends strongly on the inlet temperature T_C (the duration of the crystallization is larger when T_C is lower). The effect of the inlet velocity is very weak, so we observe no difference between the values of $\overline{\varphi(t)}$ relative to normal and inverse modes: the quasi-totality of the heat transfer is governed by natural convection.

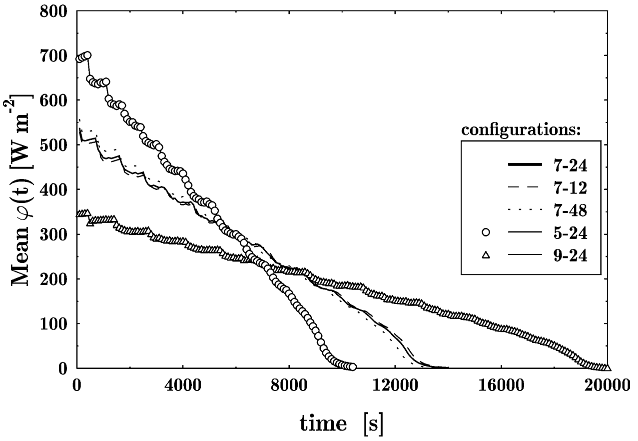

Fig. 9. Averaged heat flux (Eq. (15)) versus time for different configurations.

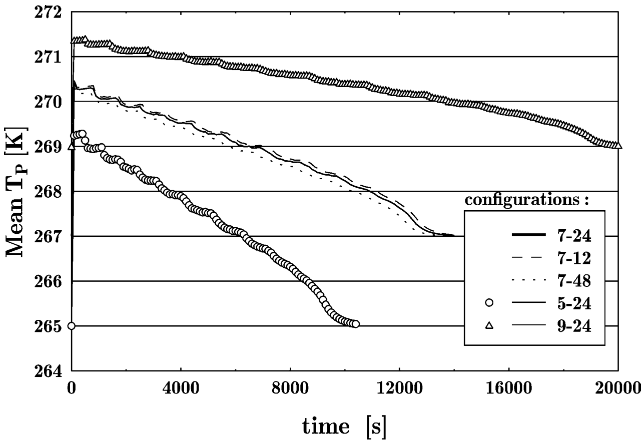

Fig. 10. Averaged external nodule temperature (Eq. (16)) versus time for different configurations.

This result is confirmed in Fig. 10 where we have plotted the mean temperature of the nodule–fluid interface defined by:

$$\overline{T_P(t)} = \frac{1}{\pi}\int_0^\pi T_P(t,\theta)\,\mathrm{d}\theta. \tag{16}$$

As stated before, liquid–solid interface can be located where the liquid fraction is $0 < f < 1$. We present in Fig. 11 the positions of this interface at different instants. We observe that these interfaces are not concentric spheres, but the asymmetry is not very important. This would explain why the quasi-stationary crystallization model [25,26], which was a concentric one, gives quite similar results.

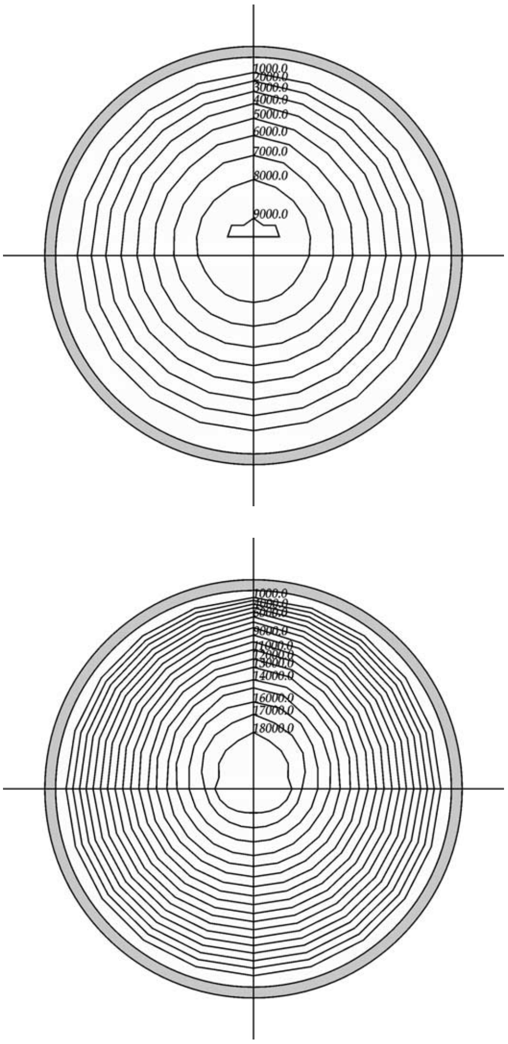

Fig. 11. Location of the liquid–solid interface versus time [s] for the configurations 5–24 (top) and 9–24.

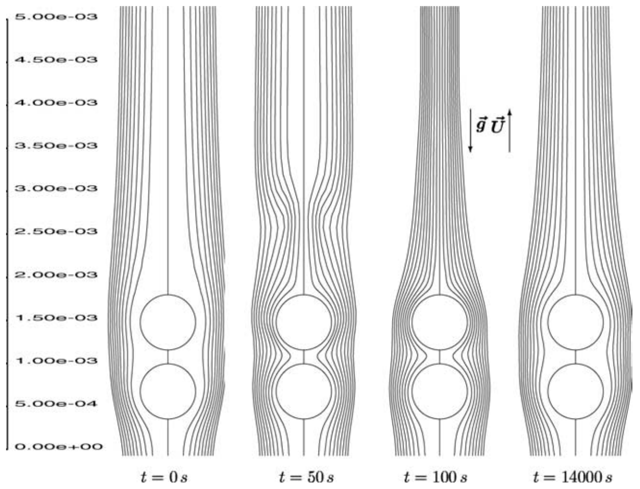

Fig. 12. Streamlines around two crystallizing nodules in normal mode [kg·s^{-1}]. (*The lowest ψ value is at the nodule surface.*)

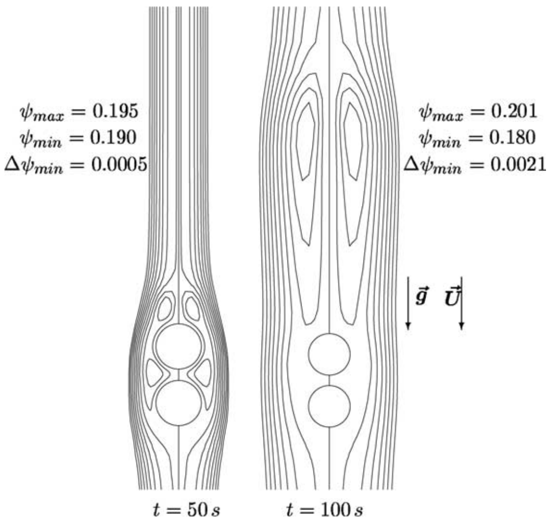

Fig. 13. Streamlines around two crystallizing nodules in inverse mode [kg·s^{-1}]. (*The lowest ψ value (ψ_{min}) is at the outer line.*)

5. Crystallization of two superposed nodules

In actual fact, the nodule is not alone in the storage tank, and the effect of the surrounding nodules is evident. To study the effect of the natural convection, we investigate the case of two superposed crystallizing nodules.

As for the previous calculations, we couple a new numerical flow simulation around two superposed nodules, with two enthalpic modules simulating the phase change inside each one of the two nodules. All the numerical considerations remain unchanged. The CFD simulation uses a new mesh that has the same nodes density near the nodules surfaces as that of the single nodule mesh.

We consider two nodules that start crystallizing at the same time. We show in Figs. 12 and 13 the streamlines obtained respectively in normal and inverse modes at different instants for the configuration 7–24. In normal mode, the trajectories have the same behavior as for a single nodule. In inverse mode, we can see two swirls—one per nodule—at early crystallization instants. Later the two swirls merge into a bigger one which is carried upward. Fluid velocities generated by the crystallization of the two nodules at the domain axis are almost two times larger than velocities generated by a single one as showed by Fig. 14.

The distribution of the heat flux on the surfaces of the two nodules are showed in Fig. 15 at time $t = 400$ s. We can see that the heat exchange at the surface of the upper nodule is weaker than that of a single nodule and especially at its bottom. As a consequence, its crystallization duration is relatively longer and its crystallization is more concentric. We deduce that even if the natural convection rising from the lower nodule increases the fluid velocity in the vicinity of the upper nodule, it does not enhance its heat exchange because the fluid is warmer.

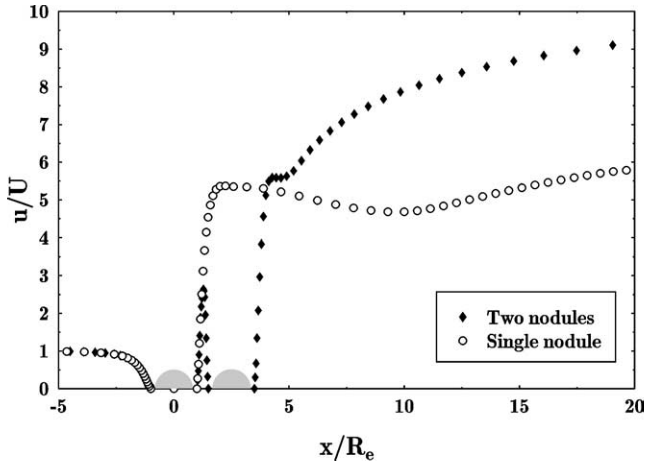

Fig. 14. Non-dimensional axial velocity on the axis at $t = 300$ s for one and two nodules (configuration 7–24).

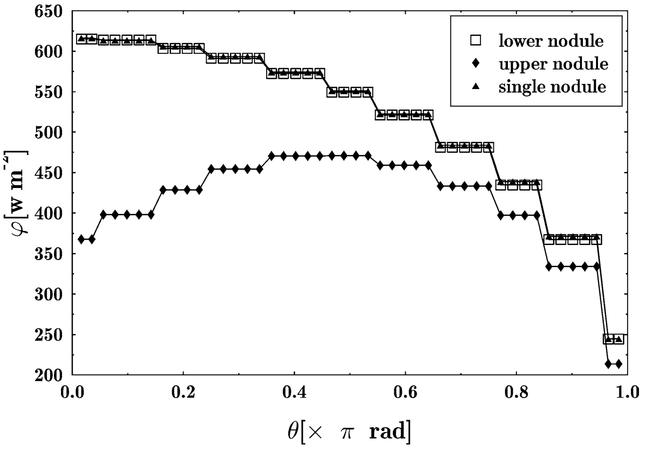

Fig. 15. Heat flux distribution on the surface of two crystallizing nodules compared to a single one at $t = 400$ s.

6. Conclusion

We have presented a numerical study of the mutual influence between the flow around a nodule containing a Phase Change Material and its crystallization after a supercooling. We were able to predict the heat flux distribution on the surface of the nodule which was strongly related to natural convection streams. We also obtained informations on the kinetics of crystallization, its duration, and the displacement of the phase change front. The application of this modelling to the case of two superposed nodules demonstrates that the crystallization of a nodule is noticeably slowed by the presence of other neighboring crystallizing nodules.

References

[1] J.P. Bédécarrats, J.P. Dumas, Study of crystallization of nodules containing a phase change material for cool thermal storage, Internat. J. Heat Mass Transfer 40 (1) (1997) 149–157.

[2] J.P. Bédécarrats, F. Strub, B. Falcon, J.P. Dumas, Phase-change thermal energy storage using spherical capsules. Performance of a test plant, Internat. J. Refrig. 19 (3) (1996) 187–196.

[3] Y.P. Shih, T.C. Chou, Analytical solutions for freezing a saturated liquid inside or outside sphere, Chem. Engrg. Sci. 26 (1971) 1787–1793.

[4] R.I. Pedroso, G.A. Domoto, Inward spherical solidification solution by the method of strained coordinates, Internat. J. Heat Mass Transfer 16 (1973) 1037–1043.

[5] D.S. Riley, F.T. Smith, G. Poots, The inward solidification of spheres and circular cylinders, Internat. J. Heat Mass Transfer 17 (12) (1974) 1507–1516.

[6] J.M. Hill, A. Kucera, Freezing a saturated liquid inside a sphere, Internat. J. Heat Mass Transfer 26 (1983) 1631–1636.

[7] K.A.R. Ismail, J.R. Henríquez, T.M. da Silva, A parametric study on ice formation inside a spherical capsule, Internat. J. Therm. Sci. 42 (9) (2003) 881–887.

[8] D.L. Feltham, J. Garside, Analytical and numerical solutions describing the inward solidification of a binary melt, Chem. Engrg. Sci. 56 (7) (2001) 2357–2370.

[9] I.W. Eames, K.T. Adref, Freezing and melting of water in spherical enclosures of the type used in thermal (ice) storage systems, Appl. Therm. Engrg. 22 (7) (2002) 733–745.

[10] D. Arnold, Dynamic simulation of encapsulated stores, part I—The model, ASHRAE Trans. 96 (1) (1990) 1245–1254.

[11] K. Cho, S.H. Choi, Thermal characteristics of paraffin in a spherical capsule during freezing and melting processes, Internat. J. Heat Mass Transfer 43 (17) (2000) 3183–3196.

[12] K.A.R. Ismail, J.R. Henríquez, Numerical and experimental study of spherical capsules packed bed latent heat storage system, Appl. Therm. Engrg. 22 (15) (2002) 1705–1716.

[13] T. Yuge, Experiments on heat transfer from spheres including natural and forced convection, J. Heat Transfer 82 (3) (1960) 214–220.

[14] B.F. Armaly, T.S. Chen, N. Ramachandran, Correlations for mixed convection flows across horizontal cylinders and spheres, J. Heat Transfer 110 (1988) 511–514.

[15] W.S. Amato, C. Tien, Free convection heat transfer from isothermal spheres in water, Internat. J. Heat Mass Transfer 15 (1972) 327–339.

[16] S.W. Churchill, Comprehensive theoretically based, correlating equations for free convection from isothermal spheres, Chem. Engrg. Comm. 24 (1983) 339–352.

[17] G.D. Kirk, A.T. Johnson, Experimental determination of mixed convective heat transfer from a sphere to air, Internat. Comm. Heat Mass 13 (4) (1986) 369–387.

[18] L. Tang, A.T. Johnson, Flow visualization of mixed convection about a sphere, Internat. Comm. Heat Mass 17 (1) (1990) 67–77.

[19] L. Tang, A.T. Johnson, R.H. McCuen, Empirical study of mixed convection about a sphere, J. Agric. Engrg. Res. 50 (1991) 197–208.

[20] T.S. Chen, A. Mucoglu, Analysis of mixed forced and free convection about a sphere, Internat. J. Heat Mass Transfer 20 (1977) 867–875.

[21] J. Potter, N. Riley, Free convection from a heated sphere at large Grashof number, J. Fluid Mech. 100 (4) (1980) 769–783.

[22] N. Riley, The heat transfer from a sphere in free convective flow, Comput. Fluids 14 (3) (1986) 225–237.

[23] H.D. Nguyen, S. Paik, J.N. Chung, Unsteady mixed convection heat transfer from a solid sphere: The conjugate problem, Internat. J. Heat Mass Transfer 36 (18) (1993) 4443–4453.

[24] H. Jia, G. Gogos, Laminar natural convection heat transfer from isothermal spheres, Internat. J. Heat Mass Transfer 39 (8) (1996) 1603–1615.

[25] K. El Omari, Étude de la convection autour d'un nodule sphérique contenant un matériau à changement de phase au cours de sa cristallisation, Ph.D. Thesis, University of Pau, 2001.

[26] K. El Omari, J.P. Dumas, Flow around a spherical nodule during its crystallization, Internat. J. Heat Technol. 21 (2) (2003) 175–182.

[27] B. Gebhart, Heat Transfer, McGraw-Hill Book, New York, 1970.

[28] Fluent Inc., Lebanon, USA, Fluent 5 User's Guide.

[29] S.R. Mathur, J.Y. Murthy, A pressure-based method for unstructured meshes, Numer. Heat Transfer B Fund. 31 (1997) 195–215.
[30] V. Patankar, Numerical Heat Transfer and Fluid Flow, Hemisphere, Washington, DC, 1980.
[31] S. Whitaker, Forced convection heat transfer correlations for flow in pipes, past flat plates, single cylinders, single spheres, and for flow in packed beds and tube bundles, AICHE J. 18 (1972) 361–371.
[32] V.R. Voller, Fast implicit finite-difference method for the analysis of phase change problems, Numer. Heat Transfer B Fund. 17 (1990) 155–169.
[33] M. Lacroix, M. Benmadda, Numerical simulation of natural convection-dominated melting and solidification from finned vertical wall, Numer. Heat Transfer A Appl. 31 (1997) 71–86.